JACS Au
AN OPEN ACCESS JOURNAL OF THE AMERICAN CHEMICAL SOCIETY

pubs.acs.org/jacsau

Letter

Transferable Deep Learning Potential Reveals Intermediate-Range Ordering Effects in LiF−NaF−ZrF_4 Molten Salt

Rajni Chahal,* Santanu Roy, Martin Brehm, Shubhojit Banerjee, Vyacheslav Bryantsev, and Stephen T. Lam*

Cite This: *JACS Au* 2022, 2, 2693−2702

Read Online

ACCESS | Metrics & More | Article Recommendations | Supporting Information

ABSTRACT: LiF−NaF−ZrF_4 multicomponent molten salts are promising candidate coolants for advanced clean energy systems owing to their desirable thermophysical and transport properties. However, the complex structures enabling these properties, and their dependence on composition, is scarcely quantified due to limitations in simulating and interpreting experimental spectra of highly disordered, intermediate-ranged structures. Specifically, size-limited ab initio simulations and accuracy-limited classical models used in the past are unable to capture a wide range of fluctuating motifs found in the extended heterogeneous structures of liquid salt. This greatly inhibits our ability to design tailored compositions and materials. Here, accurate, efficient, and transferable machine learning potentials are used to predict structures far beyond the first coordination shell in LiF−NaF−ZrF_4. Neural networks trained at only eutectic compositions with 29% and 37% ZrF_4 are shown to accurately simulate a wide range of compositions (11−40% ZrF_4) with dramatically different coordination chemistries, while showing a remarkable agreement with theoretical and experimental Raman spectra. The theoretical Raman calculations further uncovered the previously unseen shift and flattening of bending band at ∼250 cm^{-1} which validated the simulated extended-range structures as observed in compositions with higher than 29% ZrF_4 content. In such cases, machine learning-based simulations capable of accessing larger time and length scales (beyond 17 Å) were critical for accurately predicting both structure and ionic diffusivities.

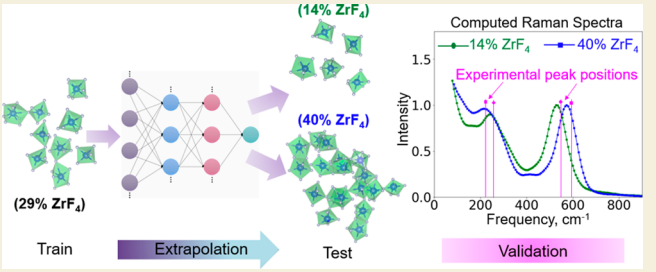

KEYWORDS: *molten salts, intermediate-range structure, diffusion coefficients, Raman spectral interpretation, ab initio molecular dynamics, polarizable ion model, transferable neural network interatomic potential, neural network molecular dynamics*

Molten salts have promising applications in advanced clean energy systems such as next-generation nuclear reactors, solar-thermal storage plants, advanced batteries, and media for carbon capture due to their desirable heat transfer properties. Fluoride salts have been previously identified as good candidates for primary coolant applications in the advanced high temperature reactor (AHTR)[1] and molten salt reactor (MSR).[2,3] Among them, ternary systems containing BeF_2 and ZrF_4 were recommended as coolant salts. While there has been a significant interest in using BeF_2-based salts due to their low neutron absorption, there remain substantial challenges in using beryllium salts due to their toxicity and required processing facilities. As such, Zr-salts present a compelling alternative due to their acceptable neutron economy, vapor pressures, thermal hydraulics, and lower costs.[3] In order to achieve low vapor pressure at higher temperatures (<1 mmHg at 700−900 °C), the ZrF_4 mole fraction in the salt mixture should be maintained within ∼20−45%.[3] Here, the eutectic compositions 26LiF−37NaF−37ZrF_4 (mol %) and 42LiF−29NaF−29ZrF_4 (mol %) with freezing point around 436 and 460 °C, respectively have been identified as promising candidates. Due to lack of data in thermophysical properties databases,[4] these salt compositions have been recommended for further study.[2]

Precise experimental interrogation of salt structure and properties is challenged by the radioactive environment, high temperature conditions, cost, materials handling, and difficulties in interpreting experimental data. Particularly, it is difficult to access the structure of multivalent cations using techniques such as Raman spectra and extended X-ray absorption fine structure (EXAFS) alone due to their existence in multiple coordination states and intermediate-range ordering.[5−7] Specifically, deducing precise local structures from ensemble-averaged Raman spectra is challenging when there is high dynamic disorder and heterogeneity in coordination environments.[8] Likewise, concerning the intermediate-range structure, a previous experimental Raman spectroscopic study by Toth et

Received: September 21, 2022
Revised: December 6, 2022
Accepted: December 6, 2022
Published: December 12, 2022

al. suggested no fluorozirconate chain formation, also known as intermediate-range ordering, even for the composition involving 40% mol content of ZrF_4.[9] However, while the local coordination states reported in this Raman study were found to be in good agreement with our previous ab initio molecular dynamics (AIMD) findings, AIMD simulations for salts with 29% and 37% ZrF_4 content revealed fluorozirconate chain formation.[10] Such an intermediate-range structural ordering effect was also previously reported from NMR and EXAFS experimental observations and classical molecular modeling for $LiF-ZrF_4$, $NaF-ZrF_4$, and $KF-ZrF_4$ salts where higher ZrF_4 mole content was present.[11,12]

In light of the challenges encountered in experimental measurements and their interpretation, AIMD simulations can be used to interpret experimental data and predict temperature-dependent structure, transport, and thermophysical properties of multicomponent molten salts.[13,14] However, accurately simulating the structure and properties of multicomponent molten salt containing multivalent cations still remains challenging due to fundamental limitations in electronic structure methods based on density functional theory (size-limited). As such, the classical molecular dynamics (CMD) simulations have been proven efficient when studying the larger system sizes. However, our previous study showed that the traditional Rigid ion model (RIM) parameters overpredict the zirconium coordination numbers as well as the intermediate-range ordering when ZrF_4 mol % is higher in the melt, which in turn lead to up to 2−3 orders of magnitude differences in the diffusion coefficients and viscosities values.[10] Such issues at higher ZrF_4 mol % content can be essentially fixed by including the polarization effects leading to the development of Polarizable ion model (PIM).[15] Here, this addition of polarization term requires accurately capturing the charge-dipole and dipole−dipole polarizability,[16] which has seen many applications in the simulation of multicomponent salts.[15,17−20]

While the fitted PIM parameters were used by Salanne et al.[21] to study electrical conductivities of molten $LiF-NaF-ZrF_4$ mixtures, a detailed study to validate the PIM-generated salt structure and transport properties using AIMD and experimental data is yet to be reported. Even though the transferability of classical interatomic potentials is an attractive trait, their further development for material screening is often overshadowed by the tedious challenges in parameter fitting, namely, ensuring excellent quality fit for both force and dipole values, the quality of experimental and first-principles data used for parameter optimization, and excessive human intervention.[15] Here, density functional theory (DFT)-accurate as well as nearly CMD-efficient neural network interatomic potentials (NNIPs) can overcome these limitations and can be trained directly on the AIMD data without requiring any significant human intervention in defining and fitting parameters that are extensible to arbitrarily complex systems. Previously, Lam et al.[22] and Chahal and Lam[23] have shown the robustness and versatility of NNIP when employed to study multicomponent molten salts containing multivalent cation species. Along this line, Rodriguez et al.[24] used the smooth edition of DeePMD-kit (DeepPot-SE)[25,26] to develop an NNIP to generate an accurate salt structure for the prediction of transport and thermophysical salt properties. As the properties such as diffusion coefficients, conductivity, and viscosity of the salt melt, etc. are strongly influenced by the formation of coordination complexes, their lifetime, and the degree of their connectivity (chain formation),[20] the NNIP transferability across different salt compositions entail the requirement for accurate prediction of short to intermediate-range structure.

It has been previously shown that the greater is the complexity of the machine learned potentials, such as in Neural network (NN) and Gaussian approximation potential (GAP), the greater is the issue with their transferability when deployed outside training thermodynamic conditions.[27] To enhance their transferability, previous studies suggested implementing an active learning loop based on the desired uncertainty quantification approach.[28−30] This further increases the complexity of NNIP development in addition to increasing the count of expensive AIMD calculations in the regions of higher uncertainty. In this Letter, we present a systematic approach for the development of NNIP trained in the limited phase-space of $LiF-NaF-ZrF_4$ salt that can accurately reproduce the short-range coordinated complexes and intermediate-range ordering effects across a wider phase-space. The fitted NNIP is used to study the short to intermediate range salt structure of five compositions of $LiF-NaF-ZrF_4$ salts: 38−51−11 (A), 40−46−14 (B), 42−29−29 (C), 26−37−37 (D) and 28−32−40 (E) mole% of $LiF-NaF-ZrF_4$ at 750 °C, 650 °C, 727 °C, 700 °C, and 550 °C, respectively. The NNIP training was performed using VASP-generated data for composition C and D at 1000K and 973 K, respectively using DeepPot-SE.[25] The DeepPot-SE model learns a mapping between local environment of each atom within 8 Å cutoff to a per-atom energy, such that the sum of atomic energies corresponds to reference DFT energy. The gradients of the NNIP-predicted energies are then used to compute the atomic forces. Both the reference energies and forces are included to evaluate the loss function which is minimized during training of an DeepPot-SE model. Specific details on the cutoff radius, network size, and tunable prefactors in loss function are provided in the Supporting Information (SI). The training data is selected based on training−validation−augmentation procedures previously used to create robust NNIPs that are able to accurately predict structures and common thermophysical properties of molten salt.[31] Specifically, it was found that, in addition to including the relaxed (near zero pressure) AIMD configurations, a few compressed and expanded configurations were also crucial to include in the NNIP training. This is also in agreement with ref 24, where the structure, transport, and thermophysical properties of LiF and $LiF-BeF_2$ molten salts were studied. Complete details of the data set for NNIP training are provided in the SI. The trained NNIP potential was then used to study the structure and ionic diffusivities for compositions A (11% ZrF_4), B (14% ZrF_4), and E (40% ZrF_4) in which the ZrF_4 content, and consequently the degree of structural ordering, is outside the range of the training data set (29% and 37% ZrF_4).

Specifically, the short to intermediate-range structure of $LiF-NaF-ZrF_4$ salt is explored using AIMD (plane wave, DZVP, TZV2P), PIM, and NN-based molecular dynamics (NNMD) simulations. The effect of increasing ZrF_4 content on the salt structure is studied. Thereafter, the appropriate cell size for each composition is explored to accurately capture the intermediate-range ordering effects in compositions containing higher ZrF_4 mol %. Further, the effect of cell parameter on the structural ordering and transport properties (self-diffusion coefficients) of the salt is discussed. The coordination states and structural ordering are validated using experimental and

https://doi.org/10.1021/jacsau.2c00526
JACS Au 2022, 2, 2693−2702

theoretical Raman spectral analysis. Here, an updated interpretation of experimental Raman spectra is provided based on the observed fluorozirconate chain formation for higher ZrF_4 content compositions in our simulations.

The trained NNIP potential is first used to study the short to intermediate range salt structure, which is validated by the Raman spectral observations. The cation−anion coordination numbers are evaluated and compared within the NNMD, PBE-D3 VASP (plane wave), Quickstep/CP2K (DZVP, TZV2P), and PIM simulations. Additional details of LAMMPS MD simulations,[32,33] DFT calculations,[22,34,35] and CP2K calculations[36,37] are provided in the SI. All methods agree well with the observations made in the Raman study which confirmed the occurrence of predominately 6- and 7-coordinated fluorozirconate complexes with a relatively small amount of 8-coordinated complexes (Figures 1b and S2). However, the

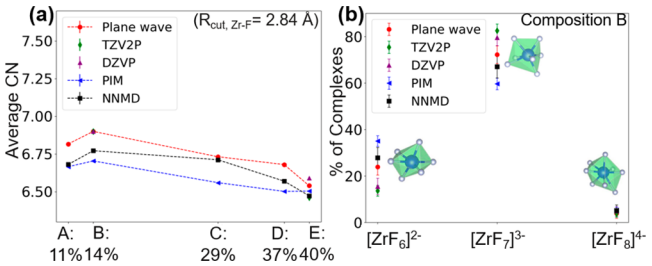

Figure 1. NNIP Transferability and comparison of local structure via (a) average F−Zr coordination number and (b) population of fluorozirconate complexes in composition B.

observed trend for the average fluoride coordination number of Zr (CN) in PIM simulations deviates from that suggested by the shift in Raman spectra, whereas both plane wave and NNMD simulations closely capture this trend (Figure 1a). In general, the shift to the higher frequency in Raman spectra indicates a decrease in the average F−Zr CN upon increasing the ZrF_4 content. This trend is generally predicted by the AIMD (plane wave, TZV2P, DZVP) and NNMD simulations for all compositions except B. The observed exception in CN trend can be explained from the perspective of difference in simulation temperatures. It is known that temperature plays a pivotal role in the F−Zr coordination number (CN increases as temperature decreases).[38] Here, the comparatively lower temperature for composition B is responsible for the slight increase in average Zr CN for composition B, which only has a slightly higher ZrF_4 content than composition A. Going from composition D to E, plane wave and NNIP simulations show a decrease in average Zr CN (in agreement with Raman spectra observation), while CMD predicted value suggests a slight increase in average Zr CN. This anomaly in average Zr CN prediction using PIM parameters was also previously reported by Pauvert et al. for a LiF−ZrF_4 system.[38]

In addition to the NNIP's ability to accurately predict the average CN, the NNMD predicted population of the 6-, 7-, and 8-fold fluorozirconate complexes show better agreement with AIMD (plane wave, TZV2P, DZVP) when compared to CMD computed values. The stability of the different coordination states in the melt can be further explored using free energy calculations. Here, while Figure 1 reveals the average coordination environment, Figure 2 illustrates distributions and metastability of different coordination structures in terms of their free energies (see SI, eq S2, for

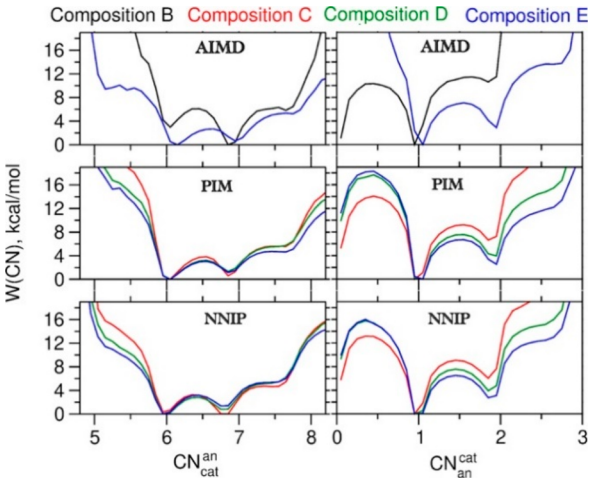

Figure 2. Free energy profiles highlighting the distributions of fluoride coordination number of Zr^{4+} (left) and zirconium coordination number of F^- for different composition with creasing zirconium content (black to blue) obtained from different molecular dynamics simulations.

definition). All simulations indicate that the fluoride coordination number of a zirconium ion is dominated by 6 and 7 while 8 is less likely to occur. The AIMD data suggests that the composition with 14 mol % Zr (composition B) prefers the 7-coordinate state more and is required to overcome a high barrier of 6 kcal/mol to transit to the 6-coordinate state. On the other hand, the composition with 40 mol % Zr (composition E) prefers the 6-coordinate state slightly more than the 7-coordinate state and the barriers between them are much smaller (2−2.5 kcal/mol), indicating their frequent interconversions. The NNIP data agree well with this preference of coordination number of Zr, even though the change in the Zr mol % is rather less drastic from composition C (29 mol %) to D (37 mol %) to E (40 mol %). The PIM data do not exhibit this sensitivity. For the zirconium coordination number of a fluoride ion, all simulations agree with the distributions of coordination numbers and their relative stabilities: the 1-coordinate state is the most-likely state while the 2-coordinate state is like to occur with increasing mol % of Zr. Here, the observed existence of 2-coordinate state corresponds to the sharing of fluorine ion among two fluorozirconate complexes leading to the intermediate-range ordering effects.

In order to explore such an intermediate-range structure formation in LiF-NaF-ZrF_4 in training (Figure 3) as well as in testing (Figure 4) regimes, Zr−Zr RDF, Zr−F−Zr angular distribution, and structure visualization (Figures 3 and 4 inset) are employed. When analyzing the Zr−Zr RDF, the first peak at ∼4 Å represents the $([ZrF_x]^{4-x})_n$ chain formation due to edge- and corner-sharing $[ZrF_x]^{4-x}$ complexes. As no first peak is observed for compositions A and B, the salt structure mainly comprises of isolated 6-, 7-, and 8-coordinated $[ZrF_x]^{4-x}$ complexes (Figure 4a, b inset). As the ZrF_4 mol % increases, the first peak in Zr−Zr RDF becomes more significant, representing an increase in fluorozirconate chain formation (Figure 3a, b inset). All the simulation methods used in this study agree well on predicting the Zr−Zr RDF at lower ZrF_4 content. However, in the cases where $([ZrF_x]^{4-x})_n$ chain formation is observed (compositions C−E), the intermediate-range ordering is more accurately predicted by NNMD when

https://doi.org/10.1021/jacsau.2c00526
JACS Au 2022, 2, 2693−2702

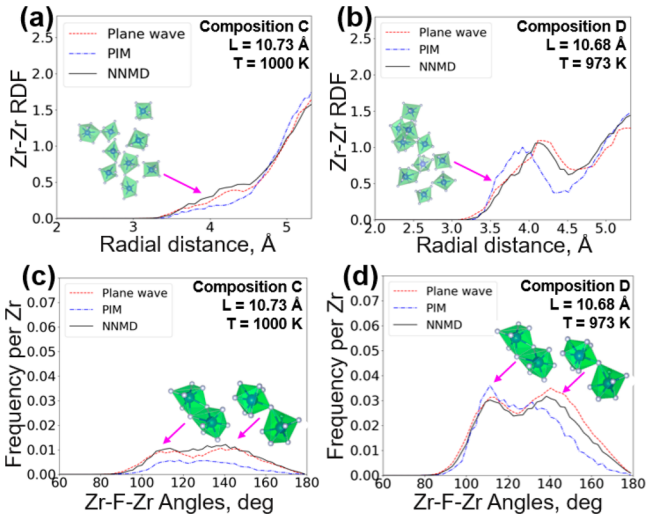

Figure 3. Comparison of NNMD-predicted (a, b) RDF and (c, d) ADF with AIMD and PIM simulations for compositions in training regime. The snapshots of the corresponding representative salt structure as viewed in VESTA[39] are shown next to the Zr−Zr first peak in Zr−Zr RDF.

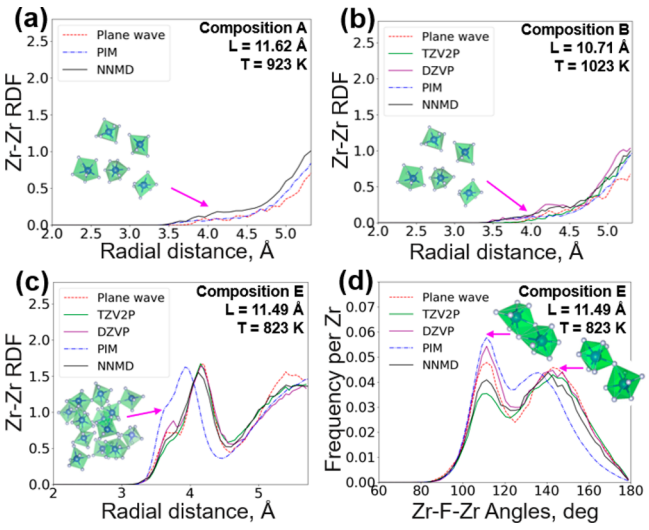

Figure 4. NNIP Transferability and comparison of intermediate-range structure ordering across a wide phase-space via (a, b) Zr−Zr RDF and (c, d) Zr−F−Zr ADF. The snapshots of the corresponding representative salt structure are shown next to the Zr−Zr first peak in Zr−Zr RDF.

compared to the PIM simulation. For composition C, PIM underpredicts the $([ZrF_x]^{4-x})_n$ chain formation (Figure 3a), which is also evident from the lower count of Zr−F−Zr in ADF (Figure 3c). As ZrF_4 mol % further increases (composition C and D), PIM generated structure is more dominated by the edge-sharing complexes, as observed from the Zr−F−Zr angles and the shift to the left in the first peak in Zr−Zr RDF. The dominant edge-sharing chain connection can be attributed to the higher F^- polarizability effect captured by PIM, which allows more shielding of Coulombic repulsive interactions between Zr−Zr from the adjacent complexes in the chain. This, in turn, decreases the Zr−F−Zr angle which leads to the decrease in Zr−Zr distance (left shift in first peak in Zr−Zr RDF). We have previously found that omitting the polarization contribution results in the chain primarily connected via corner-sharing complexes following the same reasoning provided above.[10] Here, NNMD is able to accurately predict the fluorozirconate chain connected via both corner-sharing and edge-sharing complexes for both training and test compositions.

The predicted salt structure in the simulations can be directly validated via Raman spectroscopy,[40−42] which has been traditionally employed to probe the local structure of molten salts and to understand how the structure of melts changes by varying composition and temperature. Spectral shifts in the Raman bands by varying ZrF_4 from 14 to 40% in the early work of Toth et al. were interpreted as changes in the preferred coordination of zirconium from eight to five with no fluoride bridging between Zr polyhedra. This picture was challenged and substantially refined in a more recent work of Papatheodorou and co-workers.[7] From the Raman spectra of ZrF_4−KF mixtures and related compounds they inferred a two species equilibrium between the seven- and six-coordinated zirconium ions

$$ZrF_7^{3-} \rightleftharpoons ZrF_6^{2-} + F^-$$

and a propensity of forming more extended chain structures in melts rich in $ZnCl_4$. The AIMD and NNMD generated structures in molten salts containing mostly 7- and 6-coordinate zirconium complexes (Figures 1 and 2) support the proposed equilibrium. The simulated Raman spectra (Figure 5) generated from the TZV2P basis set agree well

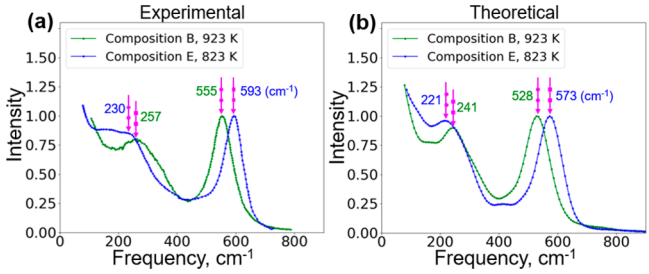

Figure 5. (a) Experimental vs (b) simulated unpolarized Raman spectra calculated using TRAVIS[42] for compositions B and E generated based on the AIMD trajectories using the TZV2P basis set. All Raman spectra are normalized for the main totally symmetric stretching band. Simulation spectra calculation details are discussed in the SI.

with the experimental spectra, both in terms of the overall shape and the shift of the main totally symmetric stretching bands to higher frequencies with increasing ZrF_4 concentration. The latter is a consequence of decreasing coordination number and increasing fluoride bridging, in which the Zr−F_t frequency with the terminal fluoride anions (F_t) is blue-shifted relative to the band of the monomeric species.[7,43] Besides the shift of the main peaks, simulations reproduce the flattening of the bending band at ∼250 cm^{-1} and the shift to lower frequencies in going from 14 to 40% ZrF_4. This is a direct result of inhomogeneous broadening associated with the depletion of the intensity coming from pure monomer species and a superposition of multiple bands at lower frequencies due to multiple chains formed by zirconium polyhedra. A shoulder in the experimental spectrum or a broader spectral feature in the simulated spectrum at ∼330 cm^{-1} in dilute $ZrCl_4$ was assigned to the E_2' vibration mode of the pentagonal bipyramidal ZrF_7^{3-} species.[7] Underestimation of the absolute

https://doi.org/10.1021/jacsau.2c00526
JACS Au 2022, 2, 2693−2702

positions of the experimental bands, which is <30 cm^{-1} in all cases, is presumably due to a slight overprediction of the stability of ZrF_7^{3-} over ZrF_6^{2-}. This underscores high sensitivity of the position of the Raman bands to changes in the coordination, providing useful experimental metrics to benchmark the accuracy of DFT in describing local structure of molten salts.

Given the formation of extended range structures as observed from simulations and interpretation of Raman spectra, the periodic boundary conditions in small simulation cell sizes can result in structural artifacts. Here, the trained NNIP potential is used to investigate the influence of simulation cell parameter on the structure and transport properties of each composition. The simulation cell size influence on the local structure is investigated using the average value of Zr CN as well as the population of existing coordination states. We found that as the cell size reaches ~12.43 Å (C), the average Zr CN and population of large $[ZrF_x]^{4-x}$ complexes increases and remains unchanged upon further increasing the cell size (Figures 6 and S3). This trend

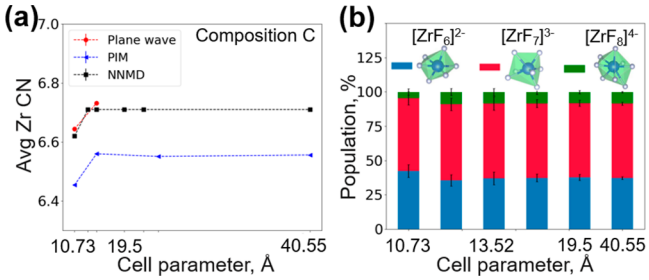

Figure 6. Exploring cell size effect of short-range structure using NNMD via (a) average Zr CN and (b) population of $[ZrF_x]^{4-x}$ complexes in composition C.

follows as observed from the plane wave AIMD values for composition C and D (Figures 6a and S3). It can be attributed to the improved averaging over an increased number of Zr complexes as the cell size increases. The inaccurate population of different coordination complexes due to restrictions on cell size and simulation trajectory length has been previously discussed in other AIMD studies.[44]

In order to explore the effect of cell parameter on the intermediate-range structure of LiF−NaF−ZrF_4, the Zr−Zr RDF, Zr−F−Zr angle distribution, and fluorozirconate cluster size ($([ZrF_x]^{4-x})_n$) distribution are employed. When a lower ZrF_4 mol % is present (compositions A and B), the Zr−Zr RDF essentially remains unchanged as the cell size increases (Figure 7a and b). Here, as no $([ZrF_x]^{4-x})_n$ cluster formation occurs, the corresponding Zr−F−Zr ADF plots are not shown. Further, as the ZrF_4 mol % increases, the first peak in the Zr−Zr RDF rapidly rises with the increase in cell size of ~10.73−12.43 Å (C) and 10.65−13.45 Å (D). This indicates an increase in the formation of more $([ZrF_x]^{4-x})_n$ clusters, which were previously restricted due to a smaller simulation cell lengths. This increase in chain formation upon larger cell length is also reflected from the increase in the frequency in Zr−F−Zr angle distribution, where the area under the curve is proportionate to the $([ZrF_x]^{4-x})_n$ clusters formed. Here, even though the $([ZrF_x]^{4-x})_n$ cluster formation changes upon a change in cell parameter, the chains stay connected via both edge- and corner-sharing complexes. The convergence of Zr−Zr RDF and Zr−F−Zr angle distribution past cell sizes of

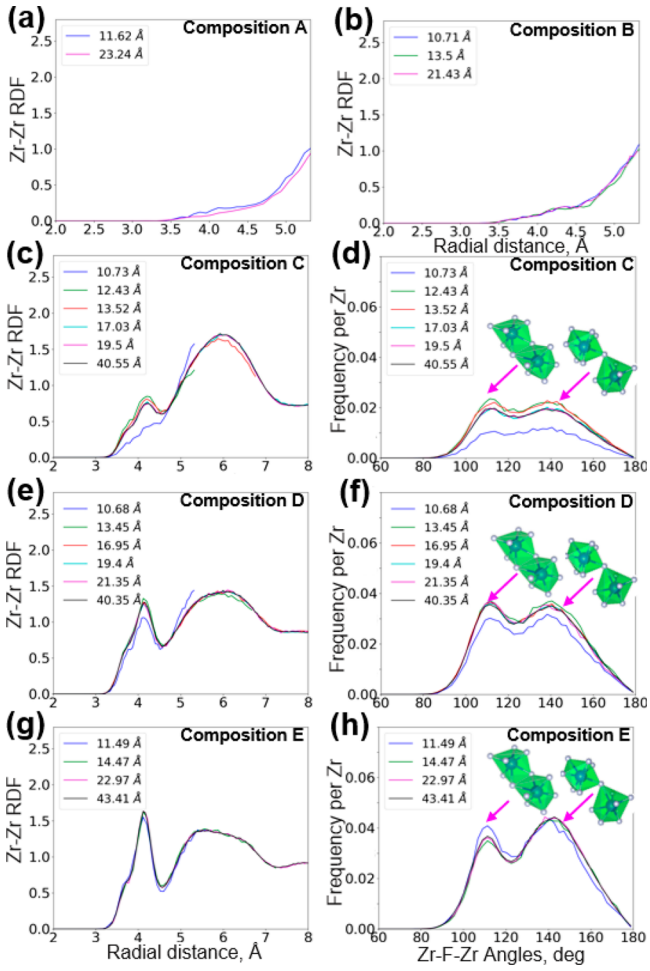

Figure 7. Exploring cell size effect on intermediate-range ordering using NNMD via (a−c,e,g) Zr−Zr RDF and (d,f,h) Zr−F−Zr angle distribution. Figure S9 shows full RDFs from large box simulations.

~12.43 Å (C), 13.45 Å (D), and 14.47 Å (E) implies these cell sizes are sufficient for the respective compositions (Figure 7). As both the Zr−Zr RDF and Zr−F−Zr angles unfold the structure up to the second coordination shell while providing only the system average, a further investigation is required to identify and quantify the $([ZrF_x]^{4-x})_n$ clusters sizes and their distribution.

In addition to dimers, we identified the $([ZrF_x]^{4-x})_n$ clusters of various sizes throughout the equilibrated trajectory by searching for their connectivity based on the cutoff value equal to Zr−F bond length (minima in Zr−F RDF = 2.84 Å). The probability of finding $([ZrF_x]^{4-x})_n$ clusters of sizes greater than 2 for compositions C, D, and E is plotted in Figure 8. Here, we noticed that even though both Zr−Zr RDF and Zr−F−Zr angles distribution converges for cell sizes ~12.43 Å (C), 13.45 Å (D), and 14.47 Å (E), the distribution of $([ZrF_x]^{4-x})_n$ clusters keep developing until cell size reaches more than nearly 17 Å (C), 21 Å (D), and 23 Å (E). Therefore, while the comparatively smaller simulation cell size is sufficient to capture the accurate salt structure in the cases where ZrF_4 is low, the cell size hinders the representation of intermediate-range structural ordering when more ZrF_4 content is present (as is the case with reactor-relevant compositions).

As the intermediate-range ordering has been previously reported to affect the transport properties like diffusion

https://doi.org/10.1021/jacsau.2c00526
JACS Au 2022, 2, 2693−2702

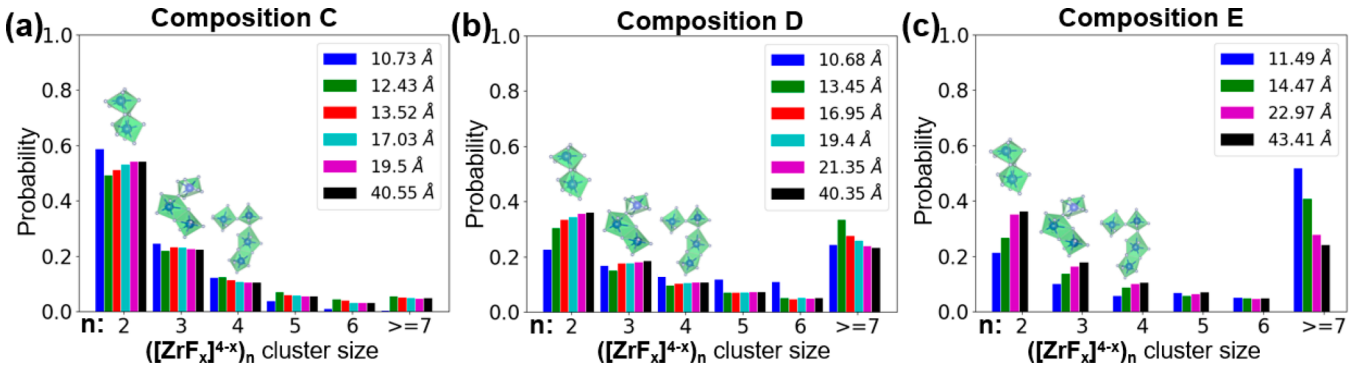

Figure 8. Appropriate cell size exploration using $([ZrF_x]^{4-x})_n$ cluster size distribution using NNMD simulations. The snapshots of cluster size 2, 3, and 4 are shown to guide the reader. Figure S10 shows snapshots of all cluster sizes. The x corresponds to 6-, 7-, and 8-coordination states of individual fluorozirconate complex ($[ZrF_6]^{2-}$, $[ZrF_7]^{3-}$, $[ZrF_8]^{4-}$).

coefficients and viscosities,[20,10] it is crucial to choose the appropriate cell parameter based on the convergence in intermediate structure ordering. It is also shown in our study by evaluating the diffusion coefficients for each cell size for the considered salt compositions using block-diffusivity method.[45] Notably, as the smaller cell sizes were sufficient to accurately represent the relatively simplified salt structure (isolated fluorozirconate complexes: $[ZrF_x]^{4-x}$) in composition A and B, the calculated diffusion coefficients are insensitive to the increase in the cell parameter (Figures 9a,c, S4, and S5). On

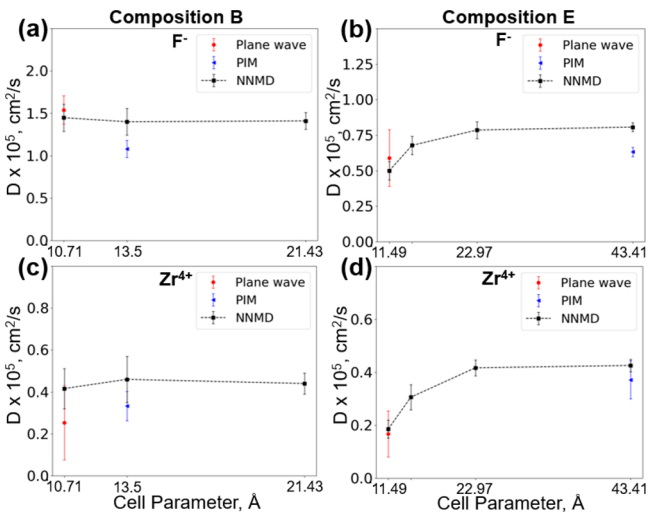

Figure 9. Effect of cell parameter on self-diffusivity using NNMD when (a) isolated $[ZrF_x]^{4-x}$ exist (composition B) and (b) extended-range structures are formed (composition E).

the contrary, when significant structural ordering effects are present, the ionic diffusion coefficients are found to vary by up to 130% as the cell sizes increase (Figures 9b,d and S6–S8). As soon as a representative cell size is attained for each composition, a plateau is observed in the values of diffusion coefficients, which agrees with our observations from the $([ZrF_x]^{4-x})_n$ cluster distribution. The observed strong agreement in the trend in convergence of different cluster sizes and the diffusivity values upon reaching a certain cell size emphasizes the significance of accurately predicting intermediate-range fluorozirconate structures toward accurate prediction of ionic diffusivities. Therefore, deciding on the appropriate cell size solely based on second coordination shell analysis (Zr–Zr RDF and Zr–F–Zr angles) would result in inaccurate self-diffusivity values. Here, it should be emphasized that such an exploration of appropriate cell sizes and calculation of long trajectories for equilibrium properties would not be feasible solely from the AIMD simulations due to limitations on practical cell size and simulation times. It can be further noticed that as the ZrF_4 mol % varies from 11% (A) to 29% (C), the self-diffusivity values drastically decrease. This is due to the formation of previously discussed intermediate-range structure motifs ($([ZrF_x]^{4-x})_n$) as ZrF_4 mol % increases. Further, the self-diffusivity values consistently decrease as the ZrF_4 mol % varies from 29% (C) to 40% (E), which can be attributed to the increase in the count of large fluorozirconate chains (e.g., $n \geq 7$) as ZrF_4 content increase from 29% to 40% (Figure 8). Such an increase in intermediate-range structural ordering is also evident from the increase in the height of first peak in the Zr–Zr RDF (Figure 7c, e, g) as ZrF_4 content increases. Overall, the observed trend in diffusivities and fluorozirconate chain formation indicates a direct relationship between the intermediate-range structural ordering and transport properties. Such differences in structure and diffusivity may further contribute to the differences in other important transport and thermophysical properties. In this respect, the effect of limited cell size on the density, heat capacity, thermal conductivity, and viscosity needs to be further studied using the developed NNIP potential. Further, it should be noted that the truncation of long-range interactions in a system may also affect property prediction. In this study, the intermediate structures, and atomic transport can be accurately predicted despite the 8 Å cutoff of the NNIP likely due to sufficient charge screening of the electrostatic potential. However, other properties and systems may be particularly sensitive to long-range interactions, including dispersion forces, or Coulomb interactions of ions separated by distances greater than the cutoff radius. In such cases, the explicit treatment of these interactions in the model should be considered.[46,47] Despite these challenges, NNIP-based modeling demonstrated here, shows significant promise in simulating a wide range of complex solvent structures, which lends itself well to compositional screening and structure–property analysis in molten salts.

Overall, this work explored the existence of structural ordering in multicomponent molten salts that is often overlooked in understanding transport property trends. Specifically, the intermediate-range ordering effects in the LiF–NaF–ZrF_4 salt were explored using the NNIP potential

https://doi.org/10.1021/jacsau.2c00526
JACS Au 2022, 2, 2693–2702

trained on 29% and 37% ZrF_4 compositions. It was found that as the mol % of multivalent cation species (ZrF_4) increases in the melt, the extended fluorozirconate chain clusters were formed, which resulted in a commensurate decrease in the ionic diffusion. Further, when such extended structures exist in the melt, a simulation cell parameter of at least 17 Å was found to be critical to correctly represent the extended-range structure as well as the ionic diffusivities. The increased simulation cell sizes, improved sampling, and DFT-level accuracy of developed NNIP allowed for an accurate prediction of intermediate-range structure and ionic diffusivities, which consistently surpassed the CMD predictions obtained using physics-based polarizable ion models. Besides the extended-range structure prediction, the developed NNIP showed excellent agreement for average coordination and the stability of 6-, 7-, and 8-coordinated fluorozirconate species when compared to ab initio calculations and Raman spectral observations. In addition to validating the NNMD predicted structure, the theoretical Raman spectral calculations also revealed the shift and flattening of the bending band at ∼250 cm^{-1}, which correspond to the structural ordering effects previously misinterpreted in the experimental spectral observations. As such, the demonstrated transferability of NNIP across a wide range of compositions (11−40% ZrF_4) and thermodynamics conditions opens up the possibility of the development of robust and reliable neural network potentials to advance the screening of new and unseen chemical compositions of many structurally complex liquids.

METHODS

Data Set Generation: AIMD Simulations

The accuracy of neural network models is limited by the quality of ab initio data used for network training and validation.[22] As such, the data for 42−29−29 and 26−37−37 mol % of LiF−NaF−ZrF_4 was taken from our previous study.[10] In brief, we performed Born−Oppenheimer AIMD simulations using the Vienna Ab Initio Simulation Package (VASP) with the projector augmented wave (PAW) method, a plane wave basis set, and the Perdew−Burke−Ernzerhof (PBE) generalized-gradient-approximation (GGA) exchange correlation functional.[34] PAW−PBE potentials provided by VASP were used for Li_sv ($1s^2 2s^1$), Na_sv ($2s^2 2p^6 3s^1$), Zr_sv ($4s^2 4p^6 4d^2 5s^2$), and F_s ($2s^2 2p^5$). A large plane wave cutoff of 650 eV with a 1e-5 eV convergence criterion for electronic self-consistent steps. A 1 × 1 × 1 k-point mesh was implemented at the gamma point. The parameters chosen yield convergence within 2 meV/atom. The density functional theory (DFT)-D3 formulation proposed by Grimmes[35] was used to account for the effect of dispersion interactions. All calculations were performed allowing for spin polarization. The canonical ensemble (NVT) using a Nosé−Hoover thermostat[33] was employed while maintaining the periodic boundary conditions. The 42 LiF-29 NaF-29 ZrF_4 data set contains 16 268 configurations with 89 atom supercells at 1000 K, whereas 26 LiF-37 NaF-37 ZrF_4 contains 11,993 configurations with 84 atom supercells at 973 K. Both the supercells were at the respective AIMD calculated densities evaluated by fitting an equation of state.[48] During network training, the data sets were shuffled and were split 80−20% for training and validation.

The training data set included 5718 8% compressed, 7123 6.83% compressed, and 6725 13.7% expanded, 16 268 relaxed configurations of 42LiF−29NaF−29ZrF_4 at 1000 K, and 11 993 relaxed configurations of 26LiF−37NaF−37ZrF_4 at 973 K. The relaxed configurations are referred to as the supercells size evaluated by fitting an equation of state. During network training, the data sets were shuffled and were split in 80% and 20% for training and validation, respectively.

CMD Simulations

Polarizable Ion Model potential is used to study the previously mentioned compositions as well. It can be noted that the simulation cell volume considered for PIM-IPMD calculations for all three compositions was 8 times that considered in AIMD (plane wave, DZVP, TZV2P) and NNMD simulations. CP2K is employed for classical molecular simulations.[36] The interatomic interactions are defined using PIM potential parameters developed by Salanne et al.[15] For direct comparison with the First-principles calculations, the simulations were also conducted for cell parameter corresponding to additive molar volume density (for Composition A) and AIMD equilibrium densities (for compositions B and C). With 2 fs as the time step, at least 2 ns simulations were performed using constant volume ensemble (NVT) using Nosé−Hoover chains thermostat[37] while maintaining the periodic boundary conditions. These simulations were used for sampling from over 4 ns trajectories each to compare the salt structure with that of AIMD calculations.

NNIP Training

For training of interatomic potential, DeePMD-kit (DP-kit) package (version 1.3.3) was employed.[25] The Deep-Pot-Smooth Edition (DeepPot-SE) potential contained inside the DP-kit was chosen due to smooth and continuously differentiable potential energy surface generation.[26] Here, the smooth cutoff and hard cutoff radius of 2 and 8 Å is chosen. The embedding network and fitting network size are {25,50,100} and {240,240,240), respectively. The tunable prefactors in loss function were chosen as 0.002, 1000, 1, 1 for p_e^{start}, p_f^{start}, p_e^{limit}, and p_f^{limit}, respectively. The network was only trained on AIMD energies and forces. The trained network using DeepPot-SE yielded energy and force errors of 2.88 meV/atom and 72 meV/Å, respectively. These errors are within the precision of DFT. The low energy and force testing errors suggest a well-fitted potential energy surface.

NNMD Simulations

The trained NNIP potential was used in Large Scale Atomic/Molecular Massively Parallel Simulator (LAMMPS) via the interface with DeePMD-kit.[32] For all compositions, the system size and simulation temperatures were chosen to be the same as that in AIMD (Plane wave, DZVP, TZV2P) and PIM simulations. With 2 fs as the time step, at least 2 ns simulations were performed using constant volume ensemble (NVT) using a Nosé−Hoover thermostat[33] while maintaining the periodic boundary conditions. The equilibrated trajectory of greater than 500 ps was used for both compositions to perform coordination and intermediate-range structure analysis.

Theoretical Raman Spectra Simulations

In our recent work,[40] we have developed a capability to simulate Raman spectra of molten salts from AIMD simulations by Fourier transformation of time autocorrelation functions involving the appropriate polarizability tensor components of the full periodic simulation cell directly from the wave function, using the correct quantum chemical operator from modern theory of polarization (Berry phase

https://doi.org/10.1021/jacsau.2c00526
JACS Au 2022, 2, 2693−2702

approach), as implemented in CP2K. Compared to previous studies, our approach does not make any assumptions about the polarizability model and can naturally account for any charge transfer and many other cooperative effects which cannot be captured well in terms of individual ions' polarizabilities. The polarizability tensor was obtained by applying an electric field (the intensity is 0.005 atomic units) along the three perpendicular axis and extracting the induced dipole moments every 4 fs over 60 ps. As the dipole vectors are based on the periodic Berry phase operator in CP2K, they are defined modulo integer multiples of the cell matrix. Whenever a large jump in the dipole moment is detected, an integer multiplier is added to ensure that the dipole moment components change smoothly with time. The time series of the polarizability tensor obtained by CP2K was used as an input to the TRAVIS program package,[41,42] to compute the Raman spectra using the correlation depth of the correlation functions of 640 fs and the laser wavenumber of 4063.21 cm^{-1}.

■ ASSOCIATED CONTENT

Data Availability Statement

The trained NNIP is made available to the community on the GitHub link: https://github.com/rajnichahal/Lam-Research-Group-Materials-Simulation/. The test and training data generated in the manuscript will be available by the authors, without undue reservation upon reasonable request.

Supporting Information

The Supporting Information is available free of charge at https://pubs.acs.org/doi/10.1021/jacsau.2c00526.

Detailed information on NNIP training and testing, investigating self-correlation effects in NNIP, methods, equations, and additional figures for diffusivity, RDF, and fluorozirconate local and intermediate-range chain structure (PDF)

■ AUTHOR INFORMATION

Corresponding Authors

Rajni Chahal − *Chemical Engineering, University of Massachusetts Lowell, Lowell, Massachusetts 01854, United States;* orcid.org/0000-0003-2190-0473; Email: rajni_chahal@uml.edu

Stephen T. Lam − *Chemical Engineering, University of Massachusetts Lowell, Lowell, Massachusetts 01854, United States;* orcid.org/0000-0002-7683-1201; Email: stephen_lam@uml.edu

Authors

Santanu Roy − *Chemical Science Division, Oak Ridge National Laboratory, Oak Ridge, Tennessee 37830, United States;* orcid.org/0000-0001-6991-8205

Martin Brehm − *Martin-Luther-Universität Halle-Wittenberg, Halle (Saale) 06120, Germany;* orcid.org/0000-0002-6861-459X

Shubhojit Banerjee − *Chemical Engineering, University of Massachusetts Lowell, Lowell, Massachusetts 01854, United States*

Vyacheslav Bryantsev − *Chemical Science Division, Oak Ridge National Laboratory, Oak Ridge, Tennessee 37830, United States;* orcid.org/0000-0002-6501-6594

Complete contact information is available at: https://pubs.acs.org/10.1021/jacsau.2c00526

Author Contributions

R.C. and S.L. conceived and guided the overall study. R.C. performed and analyzed the VASP, PIM, and NNMD simulations for all compositions. R.C. developed the NNIP potential with insights from S.L. S.R. did the free energy calculations. V.B. did TZV2P and DZVP simulations and calculated the theoretical Raman spectra using TRAVIS code developed by M.B. R.C. wrote the original manuscript, while S.R. and V.B. contributed to their respective sections in manuscript. All authors proofread, commented on, and approved the final version of the manuscript. CRediT: **Rajni Chahal** conceptualization, data curation, formal analysis, investigation, methodology, resources, validation, visualization, writing-original draft, writing-review & editing; **Santanu Roy** formal analysis, investigation, writing-review & editing; **Martin Brehm** software, writing-review & editing; **Shubhojit Banerjee** writing-review & editing; **Vyacheslav S. Bryantsev** formal analysis, investigation, methodology, validation, writing-review & editing; **Stephen Lam** conceptualization, funding acquisition, methodology, project administration, resources, supervision, writing-review & editing.

Notes

The authors declare no competing financial interest.

■ ACKNOWLEDGMENTS

This work is supported by DOE-NE's Nuclear Energy University Program (NEUP) under Award DE-NE0009204. M.B. acknowledges financial support by the Deutsche Forschungsgemeinschaft (DFG) through project Br 5494/1-3. A part of the computational resources were provided by Massachusetts green high performance computing cluster (MGHPCC). This research also used resources of the National Energy Research Scientific Computing Center, a DOE Office of Science User Facility supported by the Office of Science of the U.S. Department of Energy under Contract No. DE-AC02-05CH11231, awards ASCR-ERCAP0022362 and BES-ERCAP0022445.

■ REFERENCES

(1) Grimes, W. R.; Cuneo, D. R.; Blankenship, F. F. Chemical Aspects of Molten-Fluoride-Salt Reactor Fuels. *Fluid fuel reactors* **1958**, 569−594.

(2) Fredrickson, G. L.; Cao, G.; Gakhar, R.; Yoo, T.-S.*Molten Salt Reactor Salt Processing − Technology Status*, Aug. 2018. DOI: 10.2172/1484689.

(3) Williams, D. F.*Assessment of Candidate Molten Salt Coolants for the Advanced High Temperature Reactor (AHTR)*; Oak Ridge, TN, Mar. 2006. DOI: 10.2172/885975.

(4) Jerden, J.*Molten Salt Thermophysical Properties Database Development: 2019 Update*, ANL/CFCT-19/6, 2019. DOI: 10.2172/1559846.

(5) Roy, S.; Liu, Y.; Topsakal, M.; Dias, E.; Gakhar, R.; Phillips, W. C.; Wishart, J. F.; Leshchev, D.; Halstenberg, P.; Dai, S.; Gill, S. K.; Frenkel, A. I.; Bryantsev, V. S. A Holistic Approach for Elucidating Local Structure, Dynamics, and Speciation in Molten Salts with High Structural Disorder. *J. Am. Chem. Soc.* **2021**, *143* (37), 15298−15308.

(6) Timoshenko, J.; Anspoks, A.; Cintins, A.; Kuzmin, A.; Purans, J.; Frenkel, A. I. Neural Network Approach for Characterizing Structural Transformations by X-Ray Absorption Fine Structure Spectroscopy. *Phys. Rev. Lett.* **2018**, *120* (22), 225502.

(7) Dracopoulos, V.; Vagelatos, J.; Papatheodorou, G. N. Raman spectroscopic studies of molten ZrF4-KF mixtures and of A2ZrF6, A3Zrf7 (A = Li, K or Cs) compounds. *J. Chem. Soc., Dalton Trans.* **2001**, *7* (7), 1117−1122.

(8) Brooker, V. H. A Raman spectroscopic study of the structural aspects of K 2MgCl4 and Cs2MgCl4 as solid single crystals and molten salts. *J. Chem. Phys.* **1975**, *63* (7), 3054−3061.
(9) Toth, L. M.; Quist, A. S.; Boyd, G. E. Raman Spectra of Zirconium(IV) Fluoride Complex Ions in Fluoride Melts and Polycrystalline Solids. *J. Phys. Chem.* **1973**, *77* (11), 1384−1388.
(10) Chahal, R.; Banerjee, S.; Lam, S. T. Short- to Intermediate-Range Structure, Transport, and Thermophysical Properties of LiF−NaF−ZrF4Molten Salts. *Front. Phys.* **2022**, *10*, 830468.
(11) Rollet, A. L.; Bessada, C.; Rakhmatoulline, A.; Auger, Y.; Melin, P.; Gailhanou, M.; Thiaudière, D. In situ high temperature NMR and EXAFS experiments in rare-earth fluoride molten salts. *Comptes Rendus Chimie* **2004**, *7* (12), 1135−1140.
(12) Pauvert, O.; Salanne, M.; Zanghi, D.; Simon, C.; Reguer, S.; Thiaudière, D.; Okamoto, Y.; Matsuura, H.; Bessada, C. Ion specific effects on the structure of molten AF-ZrF4 Systems (A+ = Li+, Na+, and K+). *J. Phys. Chem. B* **2011**, *115* (29), 9160−9167.
(13) Li, Q. J.; Sprouster, D.; Zheng, G.; Neuefeind, J. C.; Braatz, A. D.; McFarlane, J.; Olds, D.; Lam, S.; Li, J.; Khaykovich, B. Complex Structure of Molten NaCl-CrCl3Salt: Cr-Cl Octahedral Network and Intermediate-Range Order. *ACS Appl. Energy Mater.* **2021**, *4* (4), 3044−3056.
(14) Nam, H. O.; Bengtson, A.; Vörtler, K.; Saha, S.; Sakidja, R.; Morgan, D. First-principles molecular dynamics modeling of the molten fluoride salt with Cr solute. *J. Nucl. Mater.* **2014**, *449* (1−3), 148−157.
(15) Salanne, M.; Simon, C.; Turq, P.; Madden, P. A. Heat-transport properties of molten fluorides: Determination from first-principles. *J. Fluor Chem.* **2009**, *130* (1), 38−44.
(16) Salanne, M.; Simon, C.; Turq, P.; Ohtori, N.; Madden, P. A. A.Modeling of Molten Salts. In *Molten Salts Chemistry*, 1st ed.; Elsevier Inc., 2013; pp 1−16. DOI: 10.1016/B978-0-12-398538-5.00001-9.
(17) Lam, S. T.; Li, Q.-J.; Mailoa, J. P.; Forsberg, C.; Ballinger, R.; Li, J. The Impact of Hydrogen Valence on Its Bonding and Transport in Molten Fluoride Salts. *J. Mater. Chem. A Mater.* **2021**, *9*, 1784−1794.
(18) Nam, H. O.; Morgan, D. Redox condition in molten salts and solute behavior: A first-principles molecular dynamics study. *J. Nucl. Mater.* **2015**, *465*, 224−235.
(19) Salanne, M.; Rotenberg, B.; Jahn, S.; Vuilleumier, R.; Simon, C.; Madden, P. A. Including many-body effects in models for ionic liquids. *Theor. Chem. Acc.* **2012**, *131* (3), 1143.
(20) Salanne, M.; Madden, P. A. Polarization effects in ionic solids and melts. *Mol. Phys.* **2011**, *109* (19), 2299−2315.
(21) Salanne, M.; Simon, C.; Groult, H.; Lantelme, F.; Goto, T.; Barhoun, A. Transport in molten LiF-NaF-ZrF4 mixtures: A combined computational and experimental approach. *J. Fluor Chem.* **2009**, *130* (1), 61−66.
(22) Lam, S. T.; Li, Q. J.; Ballinger, R.; Forsberg, C.; Li, J. Modeling LiF and FLiBe Molten Salts with Robust Neural Network Interatomic Potential. *ACS Appl. Mater. Interfaces* **2021**, *13* (21), 24582−24592.
(23) Chahal, R.; Lam, S. T. Structure Analysis of LiF-NaF-ZrF_4 Molten Salts with Deep Learning Potentials. *Trans. Am. Nucl. Soc.* **2022**, 113−116.
(24) Rodriguez, A.; Lam, S.; Hu, M. Thermodynamic and Transport Properties of LiF and FLiBe Molten Salts with Deep Learning Potentials. *ACS Appl. Mater. Interfaces* **2021**, *13* (46), 55367−55379.
(25) Wang, H.; Zhang, L.; Han, J.; E, W. DeePMD-kit: A deep learning package for many-body potential energy representation and molecular dynamics. *Comput. Phys. Commun.* **2018**, *228*, 178−184.
(26) Zhang, L.; Han, J.; Wang, H.; Saidi, W. A.; Car, R.; Weinan, E.End-to-end symmetry preserving inter-atomic potential energy model for finite and extended systems. *ArXiv (Computational Physics)*, December 20, **2018**, 1805.09003, ver. 2. DOI: 10.48550/arXiv.1805.09003.
(27) Zuo, Y.; Chen, C.; Li, X.; Deng, Z.; Chen, Y.; Behler, J.; Csányi, G.; Shapeev, A. V.; Thompson, A. P.; Wood, M. A.; Ong, S. P. Performance and Cost Assessment of Machine Learning Interatomic Potentials. *J. Phys. Chem. A* **2020**, *124* (4), 731−745.
(28) Zhang, Y.; Wang, H.; Chen, W.; Zeng, J.; Zhang, L.; Wang, H.; E, W. DP-GEN: A concurrent learning platform for the generation of reliable deep learning based potential energy models. *Comput. Phys. Commun.* **2020**, *253*, 107206.
(29) Guo, D.; Zhao, J.; Liang, W.; Lu, G. Molecular dynamics simulation of molten strontium chloride based on deep potential. *J. Mol. Liq.* **2022**, *348* (1), 118380.
(30) Guo, J.; Ward, L.; Babuji, Y.; Hoyt, N.; Williamson, M.; Foster, I.; Jackson, N.; Benmore, C.; Sivaraman, G. Composition-transferable machine learning potential for LiCl-KCl molten salts validated by high-energy x-ray diffraction. *Phys. Rev. B* **2022**, *106* (1), 014209.
(31) Li, Q.-J.; Küçükbenli, E.; Lam, S.; Khaykovich, B.; Kaxiras, E.; Li, J. Development of robust neural-network interatomic potential for molten salt. *Cell Rep. Phys. Sci.* **2021**, *2* (3), 100359.
(32) Plimpton, S. Short-Range Molecular Dynamics. *J. Comput. Phys.* **1995**, *117*, 1−19.
(33) Hoover, W. G. Canonical dynamics: Equilibrium phase-space distributions. *Phys. Rev. A (Coll Park)* **1985**, *31* (3), 1695−1697.
(34) Perdew, J. P.; Burke, K.; Ernzerhof, M. Generalized Gradient Approximation Made Simple. *Phys. Rev. Lett.* **1996**, *77* (18), 3865−3868.
(35) Grimme, S.; Antony, J.; Ehrlich, S.; Krieg, H. A consistent and accurate ab initio parametrization of density functional dispersion correction (DFT-D) for the 94 elements H-Pu. *J. Chem. Phys.* **2010**, *132* (15), 154104.
(36) Kühne, T. D.; Iannuzzi, M.; Ben, M.D.; Rybkin, V.V.; Seewald, P.; Stein, F.; Laino, T.; Khaliullin, R.Z.; Schütt, O.; Schiffmann, F.; Golze, D.; Wilhelm, J.; Chulkov, S.; Bani-Hashemian, M. H.; Weber, V.; Borštnik, U.; Taillefumier, M.; Jakobovits, A.S.; Lazzaro, A.; Pabst, H.; Müller, T.; Schade, R.; Guidon, M.; Andermatt, S.; Holmberg, N.; Schenter, G.K.; Hehn, A.; Busy, A.; Belleflamme, F.; Tabacchi, G.; Glöß, A.; Lass, M.; Bethune, I.; Mundy, C.J.; Plessl, C.; Watkins, M.; VandeVondele, J.; Krack, M.; Hutter, J. CP2K: An electronic structure and molecular dynamics software package -Quickstep: Efficient and accurate electronic structure calculations. *J. Chem. Phys.* **2020**, *152* (19), 194103.
(37) Martyna, G. J.; Klein, M. L.; Tuckerman, M. Nosé-Hoover chains: The canonical ensemble via continuous dynamics. *J. Chem. Phys.* **1992**, *97* (4), 2635−2643.
(38) Pauvert, O.; Zanghi, D.; Salarme, M.; Simon, C.; Rakhmatullin, A.; Matsuura, H.; Okamoto, Y.; Vivet, F.; Bessada, C. In situ experimental evidence for a nonmonotonous structural evolution with composition in the molten LiF-ZrF4 system. *J. Phys. Chem. B* **2010**, *114* (19), 6472−6479.
(39) Momma, K.; Izumi, F. VESTA 3 for three-dimensional visualization of crystal, volumetric and morphology data. *J. Appl. Crystallogr.* **2011**, *44* (6), 1272−1276.
(40) Roy, S.; Brehm, M.; Sharma, S.; Wu, F.; Maltsev, D. S.; Halstenberg, P.; Gallington, L. C.; Mahurin, S. M.; Dai, S.; Ivanov, A. S.; Margulis, C. J.; Bryantsev, V. S. Unraveling Local Structure of Molten Salts via X-ray Scattering, Raman Spectroscopy, and Ab Initio Molecular Dynamics. *J. Phys. Chem. B* **2021**, *125* (22), 5971−5982.
(41) Brehm, M.; Kirchner, B. TRAVIS - A free analyzer and visualizer for monte carlo and molecular dynamics trajectories. *J. Chem. Inf Model* **2011**, *51* (8), 2007−2023.
(42) Brehm, M.; Thomas, M.; Gehrke, S.; Kirchner, B. TRAVIS—A free analyzer for trajectories from molecular simulation. *J. Chem. Phys.* **2020**, *152* (16), 164105.
(43) Photiadis, G. M.; Papatheodorou, G. N. Co-ordination of thorium(IV) in molten alkali-metal chlorides and the structure of liquid and glassy thorium(IV) chloride. *J. Chem. Soc., Dalton Trans.* **1999**, *20*, 3541−3548.
(44) Roy, S.; Liu, Y.; Topsakal, M.; Dias, E.; Gakhar, R.; Phillips, W. C.; Wishart, J. F.; Leshchev, D.; Halstenberg, P.; Dai, S.; Gill, S. K.; Frenkel, A. I.; Bryantsev, V. S. A Holistic Approach for Elucidating Local Structure, Dynamics, and Speciation in Molten Salts with High Structural Disorder. *J. Am. Chem. Soc.* **2021**, *143* (37), 15298−15308.

https://doi.org/10.1021/jacsau.2c00526
JACS Au 2022, 2, 2693−2702

(45) Rapaport, D. C.*The Art of Molecular Dynamics Simulation*, 2nd ed.; Cambridge University Press, 2004; pp 121−122. [Online] Available: https://www.cambridge.org/9780521825689.
(46) Zhang, L.; Wang, H.; Muniz, M. C.; Panagiotopoulos, A. Z.; Car, R.; E, W. A deep potential model with long-range electrostatic interactions. *J. Chem. Phys.* **2022**, *156* (12), 124107.
(47) Ko, T. W.; Finkler, J. A.; Goedecker, S.; Behler, J. A fourth-generation high-dimensional neural network potential with accurate electrostatics including non-local charge transfer. *Nat. Commun.* **2021**, *12* (1), 1−13.
(48) Chahal, R.; Lam, S. T. Ab-initio Molecular Dynamics Study of LiF-NaF-ZrF4Molten Salt System. *Transactions of the American Nuclear Society* **2021**, *125* (1), 549−553.

https://doi.org/10.1021/jacsau.2c00526
JACS Au 2022, 2, 2693−2702